Pérez, JJ.; Nadal, E.; Berjano, E.; González Suárez, A. (2022). Computer modeling of radiofrequency cardiac ablation including heartbeat-induced electrode displacement. Computers in Biology and Medicine. 144:1-10. https://doi.org/10.1016/j.compbiomed.2022.105346

Computer Modeling of Radiofrequency Cardiac Ablation including Heartbeat-Induced Electrode Displacement

Juan J. Pérez[1], Enrique Nadal[2], Enrique Berjano[1], Ana González-Suárez[3,4]

[1] *BioMIT, Department of Electronic Engineering, Universitat Politècnica de València, Valencia, Spain*

[2] *Instituto de Ingeniería Mecánica y Biomecánica, Universitat Politècnica de València, Valencia, Spain*

[3] *Electrical and Electronic Engineering, National University of Ireland Galway, Ireland*

[4] *Translational Medical Device Lab, National University of Ireland Galway, Ireland*

***Corresponding author:** Dr. Ana González-Suárez, Translational Medical Device Lab, 2nd Floor, Lambe Translational Research Facility, University College Hospital Galway, Ireland. Email: ana.gonzalezsuarez@nuigalway.ie

Funding: Grant RTI2018-094357-B-C21 funded by MCIN/AEI/ 10.13039/501100011033 (Spanish Ministerio de Ciencia, Innovación y Universidades / Agencia Estatal de Investigación).

Running head: Heartbeat-induced electrode displacement in RF ablation

Conflict of interest statement: The authors have no conflicts to disclose.

Abstract

Background: The state of the art in computer modeling of radiofrequency catheter ablation (RFCA) only considers a static situation, i.e. it ignores ablation electrode displacements induced by tissue movement due to heartbeats. This feature is theoretically required, since heartbeat-induced changes in contact force can be detected during this clinical procedure.

Methods: We built a 2D RFCA model coupling electrical, thermal and mechanical problems and simulated a standard energy setting (25 W – 30 s). The mechanical interaction between the ablation electrode and tissue was dynamically modeled to reproduce heartbeat-induced changes in the electrode insertion depth from 0.86 to 2.05 mm, which corresponded with contact forces between 10 and 30 g when cardiac tissue was modeled by a hyperelastic Neo-Hookean model with a Young's modulus of 75 kPa and Poisson's ratio of 0.49.

Results: The lesion size computed in the dynamic case was 6.04 mm deep, 9.48 mm maximum width and 6.98 mm surface width, which is within the range of previous experimental results based on a beating heart for a similar energy setting and contact force. The lesion size was practically identical (less than 0.04 mm difference) in the static case with the electrode inserted to an average depth of 1.46 mm (equivalent to 20 g contact force).

Conclusions: The RFCA model including heartbeat-induced electrode displacement predicts lesion depth reasonably well compared to previous experimental results based on a beating heart model.

Key words: computer model; contact force; mechanical deformation; radiofrequency ablation.

1. Introduction

Radiofrequency (RF) catheter ablation (RFCA) is intended to treat cardiac arrhythmias by applying RF electrical currents through an active electrode at the catheter tip. Once the arrhythmia origin site has been located by electrophysiological mapping, RF electrical current flows between the active electrode and a dispersive electrode on the patient's back, creating an irreversible thermal lesion in the target zone. Computer modeling has been shown to be a valuable tool for the study of electrical and thermal performance during RF ablation, not only to treat cardiac arrhythmias [1,2], but also for other purposes, such as tumor ablation [3]. Computational modeling of mechanical problems associated with tissue heating is currently a topic of interest [4–6].

To date, RFCA computer models have considered that the active electrode is resting on the surface of the cardiac tissue and therefore remains slightly inserted. The insertion depth of the electrode in the myocardium during RFCA is known to affect thermal lesion size. The deeper the electrode is inserted, the greater the power targeted onto the cardiac tissue and the smaller the RF current shunted to the blood. In fact, catheters able to measure contact force (CF) between electrode and tissue are now in regular use in clinical practice in an attempt to take insertion depth into account [7]. The contact area between electrode and tissue, i.e. the contour resulting from applying a mechanical force on the tissue is probably much more important than CF, and is also obviously related to surface deformation [8,9], since it determines how much power is targeted on the myocardium.

Most computer models for RFCA to date assume the electrode to be inserted into the tissue and that the entire penetrating portion of the catheter makes contact with the tissue, i.e. the electrode is stuck (sharp insertion) without considering superficial deformation (e.g. [10–14]). To our knowledge, there are only five RFCA modeling studies that consider

deformation of the endocardial surface (elastic insertion) [15–19]. In the model proposed by Cao *et al* [15] the deformation was not the result of solving the mechanical problem associated with the electrode/tissue contact force but was measured from the side view of tissue deformation using X-ray projection imaging and then incorporating the contour information into the computer model. From a procedural point of view they caused surface deformation by inserting the electrode into the tissue to a known depth. Unfortunately, they did not measure the contact force associated with different insertion depths. The model proposed by Petras *et al* [16] included the surface deformation from a specific value of contact force. The relation between applied force and surface deformation was obtained for any surface point using an approximation commonly employed in the mechanical indentation problem. This meant that the mechanical governing equations were not solved, and that the electrical-thermal problem was solved only after building a 'static' deformation profile. In contrast, both Yan *et al* [17] and Singh and Melnik [18] did solve the mechanical problem associated with tissue deformation by considering the cardiac tissue as a hyperelastic material and using the Mooney–Rivlin model to characterize its stress–strain curve. Both studies modeled constant voltage ablation, unlike the currently used constant power protocol. Ahn and Kim [19] also used a hyperelastic model to analyze cardiac tissue deformation due to the catheter contact force. These mechanical models are really inspired by a static image of the electrode at a given time. In other words, despite the fact that they all have represented an advance in RFCA modeling, none has considered the dynamic behavior of the mechanical interaction, i.e. heartbeat-induced electrode displacement. Changes in the CF associated with systole-diastole heart movements are normally found during RFCA [20], and in fact in some *ex vivo* models electrode displacement has been mimicked by placing tissue samples on motorized motion-controlled platforms [21,22]. Our

goal was to build an RFCA computer model including heartbeat–induced electrode displacement and to compare the computer results with those obtained from previous experiments based on a beating heart in similar conditions of energy and contact force. To our knowledge, this is the first computer model that includes this realistic feature.

2. Methods

2.1. Model geometry

We used a limited-domain model as described in Irastorza *et al* [23]. Figure 1A shows the geometry of the model which consisted of an electrode (7 Fr, 4 mm) on a fragment of cardiac tissue surrounded by blood. The catheter was only considered to be perpendicular to the tissue, which meant the model could be two-dimensional with rotational symmetry around the catheter axis. Although other positions are possible in clinical practice, this would require a 3D model at an enormous computational cost due to the different coupled physics.

The heartbeat-induced electrode displacement was assumed to be an up-and-down vertical movement that changed insertion depth (ID) from 0.86 to 2.05 mm (measured from the tissue surface). This movement followed a sine-like time evolution with a 1 Hz frequency, which is equivalent to heart rate of 60 beats per minute. This ID range was that of a contact force ranging from 10 to 30 g measured at the plastic section of the catheter, which can be considered as moderate in clinical practice [24]. This dynamic range of ~20 g is also observed in clinical practice due to the heartbeat (e.g. see Fig. 1 of [20]). The results from this dynamic model were compared to those obtained with a static model in which the electrode remained at rest at a depth of 1.45 mm (equivalent to 20 g), which is the average position.

2.2. Governing equations

The computer model was based on a triple coupled electric-thermal-mechanical problem which was solved numerically using the Finite Element Method (FEM) with ANSYS software (ANSYS, Canonsburg, PA, USA). The governing equation for the thermal problem was the Bioheat Equation [25]:

$$\rho c \frac{\partial T}{\partial t} = \nabla \cdot (k \nabla T) + Q_{RF} + Q_p + Q_{met} \quad (1)$$

where ρ is density (kg/m^3), c specific heat (J/kg·K), T temperature (ºC), t time (s), k thermal conductivity (W/m·K), Q_{RF} the heat source caused by RF power (W/m^3), Q_p the heat loss caused by blood perfusion (W/m^3) and Q_m the metabolic heat generation (W/m^3). Both Q_m and Q_p were ignored as these terms are negligible compared to the others [25]. A quasi-static approximation was employed for the electrical problem. The magnitude of the vector electric field $\vec{E}$ as obtained from $\vec{E} = -\nabla \Phi$ (Φ being voltage) while voltage was obtained from $\nabla \cdot (\sigma(T) \nabla \Phi) = 0$ (σ being electrical conductivity). The RF heat source was then obtained as $Q_{RF} = \sigma \left| \vec{E} \right|^2$.

In order to model the vaporization in the myocardium, Eq. (1) was written as a balance of enthalpy changes instead of the energy changes proposed in [26]:

$$\frac{\partial h_t}{\partial t} = \nabla (k \nabla T) + q \quad (2)$$

where h_t is the tissue enthalpy per unit volume. This value can be determined by assessing the amount of energy deposited in the tissue when its temperature is raised from 37 ºC to values above 100 °C. According to [26], enthalpy per unit volume is:

$$h_t = \begin{cases} \rho_h c_h (T - 37), & 37 \le T \le 99\ ℃ \\ \rho_h c_h (99 - 37) + H_t \cdot \frac{(T-99)}{(100-99)}, & 99 < T \le 100\ ℃ \\ \rho_h c_h (99 - 37) + H_t + \rho_{dh} c_{dh} (T - 100), & T > 100\ ℃ \end{cases} \quad (3)$$

where the subscript *h* refers to the properties of the hydrated tissue (i.e. before reaching 99 ºC), the subscript *dh* refers to those of the dehydrated tissue, and H_t is the tissue vaporization latent heat. The partial derivative of the enthalpy in Eq. (2) can be therefore expressed as:

$$\frac{\partial h_t}{\partial t} = \begin{cases} \rho_h c_h \frac{\partial T}{\partial t}, & 37 \le T \le 99\ ℃ \\ \frac{H_t}{(1\ ℃)} \cdot \frac{\partial T}{\partial t}, & 99 < T \le 100\ ℃ \\ \rho_{dh} c_{dh} \frac{\partial T}{\partial t}, & T > 100\ ℃ \end{cases} \quad (4)$$

A complete mechanical model considering the electrode displacement caused by the myocardium movement should take the contact forces between the electrode tip and the myocardium into account. The contact forces depend on the mechanical material behavior, which depends on the material properties and on the inertial effects when dynamic effects are considered. We considered a hyperelastic mechanical model for the electrode and tissue, which could reproduce heartbeat-induced oscillatory electrode displacements. We were thus able to study the thermo-electrical effects due to the time variation of the contact area and the relative position of the electrode with respect to the tissue. Our model was quasi-static, i.e. viscosity and inertial effects were ignored. This is an approximation, since dynamic effects could appear. In mathematical terms, we modeled the large deformation elasticity problem considering the Lagrangian formulation. The solution of the elasticity problem follows by obtaining a displacement field compatible with the imposed displacements, such that the virtual work of the internal forces is the same as the virtual work of the external forces $\delta W_{int} = \delta W_{ext}$, i.e. forces applied to the body. The virtual work of the internal forces is evaluated as follows:

$$\delta W_{int} = \int_{\Omega_0} \mathbf{S}: \delta\mathbf{E}\, d\Omega \quad (5)$$

where **S** is the second Piola-Kirchoff stress tensor and $\delta\mathbf{E}$ is the Green's tensor associated to the virtual displacement. The Piola-Kirchoff stress tensor can be written as follows

$$\mathbf{S} = \frac{\partial W(\mathbf{E})}{\partial \mathbf{E}} \quad (6)$$

where W is the strain energy density function, which depends on the material considered for each solid. The metal (platinum) and polymeric components (polyurethane) of the catheter were considered as elastic solids with a Krichoff-Saint Venant material model, since their strains are small but they experience considerable displacement. The strain energy density function for this material is stated in the following equation:

$$W(\mathbf{E}) = \frac{\lambda}{2}\left(tr(\mathbf{E})^2 + \mu tr(\mathbf{E}^2)\right) \quad (7)$$

where λ and μ are the Lame's constants that can be obtained through the following formulas:

$$\lambda = \frac{Ev}{(1+v)(1-2v)} \qquad \mu = \frac{E}{2\cdot(1+v)} \quad (8)$$

where v is the Poisson's ration and *E* is the Young's modulus. The Young's modulus and Poisson's ratio were 171 MPa and 0.39 for the metal electrode (platinum), respectively, and 10 MPa and 0.4 for catheter (polyurethane), respectively [27]. For the myocardium a hyperelastic Neo-Hookean model was considered with Young's modulus of 75 kPa and Poisson's ratio of 0.49 [16]. The strain energy density function was

$$W = \frac{\mu}{2}\left(\bar{I}_1 - 3\right) + \frac{1}{d}(J-1)^2 \quad (9)$$

where the material properties are represented by *G*, the shear modulus, and *d=2/K* where *K* is the bulk modulus, $\bar{I}_1$ is the first invariant of the Cauchy-Green's strain tensor ($\mathbf{C} = 2\mathbf{E} + \mathbf{I}$) and J is the determinant of the strain gradient. Additionally, the relation between the bulk

and the Young's modulus and the Poisson's ratio of a material can be obtained with the following expression:

$$K = \frac{E}{3 \cdot (1 - 2 \cdot \upsilon)} \quad (10)$$

As a first approximation, the blood around the electrode and myocardium was assumed not to have any mechanical behavior. To simulate the movement of blood around the electrode and myocardium, a Neo-Hookean hyperelastic model was considered only for consistency in the simulation. For this, we set non-realistic mechanical material properties for the blood (Young's modulus of 2 kPa and Poisson's ratio of 0.4) with the only objective of avoiding numerical instabilities of the simulation while preserving no mechanical influence in the results. Several mechanical simulations were carried out to calibrate the model, comparing the results of the mechanical response (i.e. force applied to the electrode and displacements) with and without blood.

2.3. Electrical and thermal properties

The thermal and electrical properties of the model elements are shown in Table 1 [28,29]. The thermal properties of the plastic and metal elements of the catheter were taken from [28], while the tissue properties were taken from average values reported in the ITIS database [29]. Only blood electrical characteristics were considered since the thermal problem was not solved in this subdomain. The electrical conductivity (σ) of myocardium was considered as a temperature-dependent function as follows: it rose exponentially +1.5%/ºC from 37 to 99 ºC (0.281 S/m at 37 ºC), then decreased two orders of magnitude from 99 to 100 ºC in order to model the drastic water loss due to vaporization (we previously demonstrated that using +1.5 or +2%/ºC, or 2 or 4 orders of magnitude produces very similar results [30]), and remained constant from 100 ºC onwards. The thermal

conductivity (k) of cardiac tissue was considered to be constant until reaching 99 ºC (0.56 W/K·m), and changed once the tissue was dehydrated (see Appendix [31–34]). The parameters used to model the phase change (vaporization) were as follows: H_t was estimated as the product of the water vaporization latent heat (H_w) and the water mass fraction in the cardiac tissue (C). H_w was calculated as the product of the water vaporization latent heat (2256 kJ/kg) and water density (958 kg/m^3) (both assessed at 100 ºC [32], given a value of 2.161×10^9 J/m^3. C was considered to be 75%, which is a typical value reported for heart and muscle [35,36]). H_t was therefore $1.62\cdot10^9$ J/m^3.

A sensitivity analysis was conducted to assess the impact of the dispersion in tissue characteristics on lesion size, considering the maximum and minimum myocardium values reported in the ITIS database (0.5 and 0.6 W/m·K for thermal conductivity, 1059 and 1143 kg/m^3 for density, 3614 and 3724 J/kg·K for specific heat). [29]. Both myocardium and blood electrical conductivity were considered to have a ±10% variation, which is of the same order as the dispersions of the rest of the characteristics, even though the ITIS database does not include high frequency dispersion (500 kHz). The 20 g static case was chosen for this sensitivity analysis.

2.4. Initial and boundary conditions

The initial temperature in the entire model was 37 ºC. Fig. 1B and 1C show the electrical and thermal boundary conditions, respectively. The electrical current I_E injected at a node of the active electrode was adjusted at each time step in order to apply a constant RF power of 25 W for 30 s (note that the power value used in the simulations was reduced by 20% since the model did not include the entire torso, i.e. 20 W [23]). All the outer surfaces of the

model were set to 0 V (Dirichlet boundary condition) except the surface of the symmetry axis, which was fixed at zero electric flux (Neumann boundary condition).

For the thermal boundary conditions, a null thermal flux was used on the symmetry axis and a constant temperature of 37 ºC was fixed on the outer surfaces, which were assumed to be far enough from the ablation electrode. The initial temperature value was also 37 ºC. A 'reduced model' was used, as described in [14], which consists of not solving the blood fluid dynamics. Instead, the thermal effect of blood circulating inside the cardiac chamber was modeled by convection coefficients at the electrode–blood (h_E) and the tissue–blood (h_T) interfaces, while considering blood electrical conductivity regardless of temperature (as in Method 2 in [12]). In our study, these coefficients were calculated as in [13] for a blood flow of 0.085 m/s, simulating ablation sites with low local blood flow, as in patients with chronic atrial fibrillation and dilated atria [37]: h_E = 3346 W/m^2·K and h_T = 610 W/m^2·K. In the 'reduced model', the electrode irrigation was modeled by fixing temperature at 45 ºC only in the cylindrical zone of the electrode tip, leaving the semispherical tip free. According to [14], in comparison with the full model (which does solve the blood dynamic problem), the 'reduced model' predicts almost identical lesion depths (differences < 0.1 mm) and slightly overestimates maximum and surface widths (by ~1 and 2 mm, respectively) [14]. Note that the 'reduced model' as described in [14] did solve the thermal problem in the blood subdomain, so that we also compared both 'reduced models', i.e. with and without solving the thermal problem in the blood. Although we barely found differences in lesion depth (< 0.05 mm), interestingly, the maximum and surface widths were 0.5–0.9 mm and ~2 mm smaller when the blood thermal problem was not solved (as in the present study). This suggests that not including blood in the thermal problem can obtain values similar to those obtained when fluid dynamics is included.

Fig. 1D shows the boundary conditions for the mechanical problem, specifically the displacement values in both axes (Ux and Uy) at relevant key points. We chose to use electrode displacement as load instead of CF for simplicity. Note that since the viscous behavior was not included, there is a direct and one-to-one relationship between CF and electrode vertical displacement. To state this relationship we first solved the static mechanical model for the three contact force values (10, 20 and 30 g) and obtained their corresponding displacement values on ANSYS, using a structural model and steady-state analysis (which means inertial forces and damping forces are ignored). The resulting electrode displacement values were used as peak values of the sinusoidal-waveform dynamic load applied on the catheter for the transient analysis. Figure 2 shows the consecutive time phases considered in each transient simulation (63 s in total): 1-s landing (the electrode comes into contact with the tissue surface), 30-s ablation (the electrode deforms the tissue surface by entering between 0.86 mm and 2.05 mm in the dynamic case –equivalent to a range of between 10 and 30 g of contact force) or remains steady at a depth of 0.86, 1.46 or 2.05 mm in the static cases (with contact forces of 10, 20 and 30 grams, respectively), 1-s takeoff (the electrode separates from the tissue), 30-s post-ablation (RF-off, in this period the lesion grows due to thermal latency), and 1-s landing (the electrode comes back into contact with the tissue surface). This last phase was simply conducted to measure the lesion size at the end of post-ablation period with the electrode inserted in the tissue.

The mechanical model was completed by considering the specific contact conditions between the three materials (electrode, myocardium and blood). The contact between electrode and myocardium considered the standard formulation with Signorini's boundary conditions (i.e. avoiding penetration between surfaces, computing the surface pressure that

guarantees no penetration condition, and allowing free separation) [38]. The contact between blood and myocardium followed a non-separation rule based on avoiding penetration between the materials, computing the surface pressure that guarantees no penetration condition, and once contact was established separation was not possible, thus normal tractions could be considered. Finally, a non-frictional contact model was used allowing free slip behavior between any pair of materials.

2.5. Model verification

Cardiac tissue and blood chamber dimensions (S in Fig. 1A) were previously estimated by means of a convergence test to avoid boundary effects and a value of S = 4 cm was found appropriate [23] using the value of the lesion depth (D) after 30 s of RFCA as a control parameter. Discretization was spatially heterogeneous: the finest zone was always the electrode-tissue interface with the largest voltage gradient and hence the maximum value of current density. The grid size was gradually increased in the tissue with distance from the electrode-tissue interface. We first considered a tentative spatial (i.e. minimum meshing size) and temporal resolution and determined the appropriate spatial resolution by means of a similar convergence test using the same control parameter as in the previous test. The mesh size was assumed to be suitable when an asymptotic tendency was seen in the lesion depth as mesh size decreased.

2.6. Output variables

The Arrhenius damage model was used to estimate lesion size from the temperature evolution computed at any point. This model associates temperature with exposure time by means of a first-order kinetics relationship:

$$\Omega(t) = \int_0^t A e^{-\frac{\Delta E}{R \cdot T}} ds \qquad (11)$$

where R is the universal gas constant (8.314 J/K mol), A (7.39×10^{39} s^{-1}) is a frequency factor and ΔE (2.577×10^{5} J/mol) is the activation energy for the irreversible damage reaction [28]. Lesion contour was estimated using the $\Omega = 1$ isoline.

A 'footprint' is usually observed after ablation in both the thigh muscle model [37] and the beating heart model [24], possibly due to myocardium viscosity and to the stiffer tissue after denaturing. Since our model did not consider either of these two characteristics, the only way to mimic the footprint was to measure lesion size while the electrode was inserted, i.e. we measured the lesion depth (since the tissue surface, i.e. D in Fig. 1A), surface (SW) and maximum width (MW) after the post-RF period at two almost simultaneous times: at 62 s when the electrode remained withdrawn (0 g contact force) and 1 s later (i.e. t=63 s) when the electrode was once more inserted to the same depth as during ablation (1.46 mm in the dynamic case). Note that although a few studies have measured lesion depth from the lowest point of the electrode (e.g. [16]), most do so from the tissue surface, as was done here.

3. Results

3.1. Verification of the model

The model had 7,791 nodes and 3,044 triangular elements. When the outer dimension (parameter S in Fig. 1A) was enlarged to 8 cm, the number of nodes and elements slightly varied to 8,709 and 3,422, respectively, but the change in lesion depth stayed below 0.22 mm and the maximum tissue temperature varied less than 1 ºC. Likewise, when the grid size was drastically reduced (around 30,000 nodes and more than 12,000 elements), lesion

depth varied less than 0.02 mm and the maximum tissue temperature less than 0.5 ºC. The former values of mesh size and outer dimensions were thus considered to be suitable.

3.2. Comparison between static and dynamic contact force

Table 2 shows the depth (D), surface width (SW) and maximum width (MW) of lesions computed for the static and dynamic cases. There is hardly any difference between the measurements computed with the electrode inserted and withdrawn (see Fig. 3): less than 0.3 mm for depth and 0.12 mm for widths. These values can be considered insignificant since they are less <0.5 mm, which is approximately that of the deviation observed in experimental RFCA studies [12]. The lesion size obtained from the 20±10 g dynamic model was practically identical to that of the 20 g static model (differences less than 0.04 mm in depth and 0.02 mm in widths). Lesion size increased slightly when contact force was raised from 10 to 30 g: depth increased from 5.31 to 6.64 mm, maximum width from 8.64 to 10.22 mm, and surface width from 6.48 to 7.44 mm (measurements conducted with inserted electrode).

The dynamic performance of the temperature distributions in the myocardium is given in the Supplementary Material (video file in which the first 1-s landing phase is not shown since it was due to the mechanical bond between model elements). Figure 4 shows the temperature distributions at different times during ablation (up to 30 s) and post-ablation for the dynamic case with CF of 20±10 g. As can be seen in Fig. 4 and the video file (Supplementary Material), as the electrode periodically pushes the tissue, the nodes move with this deformation so that the entire temperature distribution oscillates slightly. The evolution of the temperature at a specific depth from the tissue surface will also have small superimposed oscillations.

The raw data associated with the sensitivity analysis on the impact of dispersion in tissue thermal and electrical characteristics on lesion size are shown in the Supplementary File (Excel). To sum up, considering these static and dynamic dispersions had little impact, since the maximum difference in any lesion size (D, MW and SW) between using average and maximum/minimum values was less than 0.25 mm.

3.3. Effect of modeling hydrated tissue

The model considered different values of thermal conductivity (k) and specific heat (c) for the myocardium before and after dehydration (see Appendix and Table 1). We repeated the computer simulations for the dynamic case keeping the same values of k and c above and below 100 ºC (i.e. 0.56 W/m·K and 3686 J/kg·K, respectively), obtaining differences in lesion size below 0.03 mm (note that c always increased between 99 and 100 ºC to model the latent heat associated with the phase change).

4. Discussion

4.1. Effect of heartbeat-induced electrode displacement

The aim was to build an RFCA computer model including heartbeat-induced electrode displacement. Until now, none of the models including mechanical tissue deformation considered the dynamic changes associated with the heartbeat [16–19]. While these changes can be noted in clinical practice and appear as variations in the contact force measured by the sensor at the tip of the catheter [20], our simulation results suggest that they have a limited impact on lesion size, although the temperature map in the tissue oscillates slightly so that the temperature at a given depth will also experience oscillations. We previously observed similar behavior in another simulation context in a study in which

the applied RF voltage was oscillating at a low frequency (around 1 Hz) [39]. There we found that even though the temperature at a given depth oscillated with the oscillating RF voltage, the resulting lesion size was practically the same as when the oscillations were not considered. Our results thus suggest that in the specific case of moderate contact force (<30 g) and a standard energy setting (e.g. 25 W for 30 s) the dynamic and static model compute similar lesion size. This could be an advantage in terms of computational cost, since a model including the electrode displacement takes ~16 hours of simulation (the results file occupies 6 GB) while a static model only takes 30 min (the results file occupies 155 MB).

4.2. Comparison with experimental data

Table 3 compares lesion sizes computed with the dynamic model (mean and standard deviation from the sensitivity analysis) and previous experimental results based on a beating heart model. The experimental data were chosen from those with similar contact force, power and duration [24,37,40]. The three lesion measurements computed with the dynamic model are within the reported experimental measurement ranges. We also found reasonable agreement between our computational results and those reported by Shah *et al* [22] in an *in vitro* model that mechanically simulated catheter displacement under conditions roughly similar to ours: perpendicular catheter, 20 W, 50 cycles/minute reaching a peak “systole” of 20 g and a nadir “diastole’ of 10 g. Shah *et al* concluded that contact force–time integral (FTI) is a predictor of lesion depth at constant RF power in a contractile bench model simulating the beating heart. In terms of FTI, our model predicts a lesion depth of 6.64 mm for FTI of 900 g·s (static case with 30 g and 30 s) and ~6.00 mm for FTI of 600 g·s (static case with 20 g and 30 s, and dynamic case with 20±10 g and 30 s), while Shah *et al* reported a value ~ 6 mm for FTI of 900 g·s and ~5.2 mm for FTI of 600 g·s.

Note that although they used 60 s ablations and we simulated only 30 s, using FTI allows the comparison.

No specific experimental data are available as regards comparing the static and dynamic cases. Although Shah *et al* [22] compared the lesion sizes of static contact and variable/intermittent (dynamic) contact, both groups had really very different FTI values, with significant differences in lesion size. However, Leshem *et al* [40] did find similar lesion depths from a non-beating model based on thigh muscle and a beating heart model (both *in vivo*) in case of standard energy setting (30 W for 30 s), which does suggest that the static and dynamic models might be equivalent in terms of predicting lesion depth in the case of standard energy setting.

Finally, we found that lesion depth is relatively independent of electrode insertion depth when measured from the electrode tip rather than from the tissue surface, and obviously with the electrode inserted (see D* in Fig. 3). Specifically, D* values were 4.55, 4.62 and 4.61 mm for the static case with contact forces of 10, 20 and 30 g, respectively. Interestingly, the difference between the D* values and those shown in Table 2 for the inserted electrode (i.e. D values) is due almost entirely to the insertion depths, i.e. 0.86, 1.46 and 2.05 mm for the static case with contact forces of 10, 20 and 30 g, respectively. This is reasonable because no pressure-dependence of the electrical and thermal conductivity was considered. Within the ranges considered this suggests that no matter how much force the electrode exerts on the tissue, the thermoelectric result around the electrode is practically the same, so that lesion depth is almost the same in terms of compressed tissue when measured from the electrode tip. In this regard, Ikeda *et al* [24] found by regression that lesion depth increases by 0.09 mm/g. From our data in Table 2 we can deduce that the electrode is inserted 0.06 mm/g, and therefore the lesion depth measured

from the surface also increases 0.06 mm/g, a very similar result to the experimental findings in Ikeda *et al*. It should be remembered that for each gram of contact force, the increase in insertion depth is directly related to tissue elasticity, i.e. to its Young's modulus. If we had used a lower value than E = 75 kPa we could have found increased lesion depths around the values reported by Ikeda *et al*.

4.3. Comparison with previous computational studies

As regards previous computational modeling studies that included mechanical deformation there is also some consistency with the data reported by Petras *et al* [16]. While our results show an increased lesion depth of 1.33 mm when CF is raised from 10 to 30 g, their *ex vivo* and computational experimental results (at 20 W−30 s) rise by 0.8 mm when CF goes from 10 to 20 g, and 1 mm when it increases from 10 to 40 g. The differences could be due to the way of quantifying lesion size, since the depth values reported by Petras *et al* (2.3–3.3 mm) seem peculiarly small compared to those obtained experimentally in other experimental studies using 20 W-30 s (~4 mm), for example in Guerra *et al* [41]. It is not possible to make a direct comparison with the computational results of Yan *et al* [17] as they modeled a constant voltage ablation. However there is also some consistency, since they found that lesion depth increased by 0.85 mm when CF went from 10 to 30 g (variable power between 27 and 30 W for 30 s). Nor can we compare them with Singh and Melnik's results [18] since they did not report lesion depths and their ablations lasted twice as long (60 s). Nor can we compare them with Ahn and Kim's results [19] since they used a level of power much lower than the one used in the clinic (<10 W).

4.3. Limitations of the study

Firstly, only a perpendicular positioned catheter was considered, which allowed axial symmetry and simplified the problem to a 2D model (although other positions are possible in clinical practice, considering them would need a 3D model). It is reasonable to assume that different positions would involve different contact forces, contact areas and so different lesion size values, however, a recent ex vivo model-based study concluded that while lesion size is strongly correlated with contact force and even more strongly correlated with contact area, the correlation with catheter position is moderate-weak [9]. In fact, we found similar qualitative behavior between contact force and lesion depth, regardless of catheter position, which suggests that the simplification of assuming only a perpendicular catheter should not invalidate our conclusions in terms of comparing the static and dynamic cases. The lesion depths measured by Masnok and Watanabe [9] for a perpendicular catheter (30 W, 30 s) were quite similar to those of our static model (4.49±0.38, 5.80±0.50 and 6.31±0.68 mm for contact forces of 10, 20 and 30 g, respectively, vs. 5.31, 6.00 and 6.64 mm) (see Table 2).

Secondly, since there is still no mathematical model of the behavior of the gas bubbles formed in tissue at high temperatures that cause steam pops at a temperature of 100 ºC, our model cannot predict this phenomenon. Instead, we modeled the behavior of tissue around 100 ºC using state-of-the-art mathematical RFCA modeling, i.e. a drop in electrical conductivity to model tissue desiccation, and the enthalpy method to model the energy balance associated with phase change (vaporization). Although our computer simulations did not stop when tissue temperature reached 100 ºC, these two features kept the maximum temperature below 105 ºC and predicted lesion depth reasonably well compared to previous experimental results based on a beating heart model and similar conditions [24,37,40]. Interestingly, steam pop incidence was very low in these experimental results: 13% in Ikeda *et al* [24] and none in Leshem *et al* [40] and Nakagawa *et al* [37]. Although this is

somewhat speculative, we think that the specific conditions we simulated, i.e. a standard energy setting (25 W for 30 s) and moderate contact force (<30 g), are not liable to superheat and cause detectable/audible steam pops (even though a relatively large tissue area reached 100 ºC during the simulations, as shown in Fig. 4). In contrast, Ikeda *et al* [24] did report increased incidence of steam pops at a higher power (40 W) and greater contact force (50–100 g). It is important to point out that our conclusions are therefore only valid for conditions not prone to overheating.

Thirdly, the fluid dynamics problem was not solved in the blood. Instead, we used a 'reduced model' as described in [14], which, even though it tends to overestimate surface and maximum widths by 1–2 mm at a blood velocity of 8.5 cm/s, our complementary simulations (described in Section 2.4) suggest that having excluded the blood subdomain from the thermal problem, the lesion sizes are quite similar to those obtained with a 'full model', which did solve fluid dynamics. Obviously, any 'reduced model' is limited in not being able to predict blood temperature (which was not required in the context of the present study) and neither is it suitable for cases with high CF high or partially blocked irrigation holes by tissue [8]. Our conclusions should therefore be considered valid only at low contact forces and unhampered irrigation.

Fourthly, only contact force variations were associated with heartbeats, since they are more relevant than others such as breathing. Only a frequency of 60 beats per minute (normal rhythm) and a sinusoidal waveform were simulated. This waveform was chosen since it is easy to synthesize mathematically for application as a time-changing boundary condition. Although the actual CF evolution shows a waveform a bit more pointed than a simple sinusoidal [42], we think that there is quite a reasonable similarity between both waveforms and that the choice of a sinusoidal is a good approximation that should not

invalidate the conclusions. From a physical point of view, it is reasonable that the fluctuations due to the respiratory cycle will have a qualitative similar thermal impact to those due to heartbeats, so that the conclusions should remain valid when including electrode displacement induced by respiratory movements.

Fifthly, the model only considered the electrode's vertical displacement, i.e. as up-and-down. Horizontal movements would tend to slide the electrode over the point to be ablated, possibly reducing the effectiveness of the heating. In fact, this slippage has already been reported by Kalman *et al* [43] as occurring during large respiratory excursions or with systolic movement of the heart during the cardiac cycle. In that case, the sliding catheter was marked by fluctuations in temperature measured by the sensor embedded in the electrode and occurred especially with poor electrode-tissue contact. A later study by Chick *et al* [44] used an experimental model based on a thermochromic gel phantom to assess the effect of lateral slippage. They only considered a horizontal catheter with a low contact force of 10 g, and found a small variation in contact force (1 g) during lateral sliding movements even though they were at a distance of up to 9 mm. This range of contact force does not agree with the dynamic range found in clinical practice due to heartbeats, which is much higher (around 20 g) [20], which suggests that up-and-down displacements (i.e. normal to the tissue surface) could affect the contact force much more than lateral slippage. To drastically reduce computational complexity and cost, our model only considered up-and-down movements and a perpendicular catheter, since it allowed us to have rotational symmetry and to be able to work with a 2D model, while horizontal movements would have required a 3D model, with a huge increase in complexity, given the three coupled physics. Despite this limitation, we consider that lateral movements would have little effect on lesion depth. As expected, Chick *et al* [44] found reduced lesion depth and increased

width (actually surface length) as lateral displacement increases (which makes physical sense, since the power is applied over a larger area, or in other words is targeted for a shorter time onto the same point). The reason for this is that while Kalman *et al* [43] found that more than 80% of the horizontal displacements (induced by heartbeats and respiration) were less than 5 mm, Chick *et al* reported a reduction in lesion depth of less than 0.7 mm for the same displacement range, which can be considered insignificant in clinical terms.

And sixthly, viscous behavior was not included in the mechanical model. Although biological tissues are known to have a viscous component, it has been found that for cardiac muscle and for a mechanical excitation up to 3.5 Hz, the value of losses due to the viscous component in relation to the elastic component is only 17.5%, suggesting that the behavior is essentially elastic [45]. Other authors obtained even lower values by means of "ultrasound vibrometry" techniques using a Kevin-Voigt mechanical model and deduced that to obtain the same losses due to the viscous and elastic components, the frequency of the mechanical disturbance should be 104.4 Hz during diastole and 808.8 Hz during systole (much larger values than the heart rate, 0.5–3.5 Hz [45]).

5. Conclusions

We developed an RFCA dynamic model including heartbeat-induced electrode displacement at a standard energy setting and moderate contact force. The model predicts lesion depth reasonably well as compared to previous experimental results based on a beating heart model. Under these specific conditions, the lesion size computed by a dynamic model was practically identical to that of a static model in which the electrode remained constantly inserted at an average depth.

Appendix. Thermal characteristics for dehydrated tissue

Once the temperature reached 100 ºC, we assumed that the tissue lost its aqueous component and became dehydrated. The specific heat, thermal conductivity and density of dehydrated tissue are shown in Table 1. These were estimated as described in this Appendix. In all that follows, the subscript *w* refers to the properties of water, *dh* to dehydrated tissue, and the absence of subscript to hydrated tissue (whose characteristics are shown in the Table 1). Let us assume that in 1 kg of hydrated tissue we have *C* kg of water and (1–*C*) kg of dehydrated tissue, so that the volume (*V*) of each of the parts is:

$$V_w = \frac{m_w}{\rho_w} = \frac{C}{\rho_w}; \qquad V_{dh} = \frac{m_{dh}}{\rho_{dh}} = \frac{1-C}{\rho_{dh}} \qquad (A1)$$

The volume of hydrated tissue will be the sum:

$$V_t = \frac{C}{\rho_w} + \frac{1-C}{\rho_{dh}} \qquad (A2)$$

Consequently, tissue density will be:

$$\rho = \frac{1kg}{V_t} = \frac{1}{\frac{C}{\rho_w} + \frac{1-C}{\rho_{dh}}} \qquad (A3)$$

and density of hydrated tissue will be:

$$\rho_{dh} = \frac{1-C}{\frac{1}{\rho} - \frac{C}{\rho_w}} = \frac{0.25}{\frac{1}{1081} - \frac{0.75}{1000}} = 1428\,\frac{kg}{m3} \qquad (A4)$$

Since the specific heat measures the energy needed to raise a 1 ºC of matter, if we have 1 kg of (hydrated) tissue, *C* kg is water and (1–*C*) kg is dehydrated tissue. If we increase the tissue temperature by 1 ºC we can separate the energy needed for each component (water and dehydrated tissue) as follows:

$$c \cdot 1\ \text{kg} \cdot 1\ ℃ = c_w \cdot C\ \text{kg} \cdot 1\ ℃ + c_{dh} \cdot (1 - C)\text{kg} \cdot 1\ ℃ \qquad (A5)$$

where we can obtain the specific heat of dehydrated tissue:

$$c_{dh} = \frac{c - c_w \cdot \mathrm{C}}{(1 - \mathrm{C})} = \frac{3686 - 4090 \cdot 0.75}{(1 - 0.75)} = 2474 \frac{J}{kg \cdot K} \quad \text{(A6)}$$

The thermal conductivity of dehydrated tissue was estimated using the models described by Carson [31] for the equations of non-frozen and non-porous food (since k_w/k_{dh} was ~3, as demonstrated below). Although Carson describes several models for this particular case, he also recognizes that similar results are obtained regardless of the one used. For this reason, we used the 'parallel model', where k can be expressed as:

$$k = \sum_i k_i \cdot C_{Vi} \quad \text{(A7)}$$

where k_i is the thermal conductivity of each constituent and C_{Vi} the volumetric ratio in the mixture. Firstly we must calculate the volumetric ratio of water from the mass fraction (C):

$$C_V = \frac{\rho}{\rho_w} \cdot C = \frac{1081}{1000} \cdot 0.75 = 0.81 \quad \text{(A8)}$$

and then apply the parallel model

$$k = k_w \cdot C_V + k_{dh} \cdot (1 - C_V) \quad \text{(A9)}$$

where k_w = 0.624 W/m·K [32], to finally obtain the thermal conductivity of dehydrated tissue (data assessed at 37 ºC)

$$k_{dh} = \frac{k - k_w \cdot C_V}{(1 - C_V)} = \frac{0.56 - 0.624 \cdot 0.81}{(1 - 0.81)} = 0.287 \frac{\mathrm{W}}{\mathrm{m \cdot K}} \quad \text{(A10)}$$

which provides a relation k_w/k_{dh} = 2.17 and suggests that the chosen model is suitable because it is close to 3. This decrease in thermal conductivity once tissue is completely dehydrated is qualitatively consistent with reports from experimental studies using liver (from 0.5 to 0.19 W/m·K) [33] and swine left ventricle samples (from 0.61 to 0.50 W/m·K) [34] as used in previous numerical studies [26,33].

References

1. Iasiello M, Andreozzi A, Bianco N, Vafai K. The porous media theory applied to radiofrequency catheter ablation. Int J Numerical Methods for Heat & Fluid Flow. 2020;30(5):2669-2681. doi:10.1108/HFF-11-2018-0707.
2. Singh S, Melnik R. Thermal ablation of biological tissues in disease treatment: A review of computational models and future directions. Electromagn Biol Med. 2020 Apr 2;39(2):49-88. doi: 10.1080/15368378.2020.1741383.
3. Tucci C, Trujillo M, Berjano E, Iasiello M, Andreozzi A, Vanoli GP. Pennes' bioheat equation vs. porous media approach in computer modeling of radiofrequency tumor ablation. Sci Rep. 2021 Mar 5;11(1):5272. doi: 10.1038/s41598-021-84546-6.
4. AlAmiri A, Khanafer K, Vafai K. Fluid-structure interactions in a tissue during hyperthermia. Numerical Heat Transfer, Part A: Applications, 2014;66(1), 1-16.
5. Chung S, Vafai K. Mechanobiology of low-density lipoprotein transport within an arterial wall—impact of hyperthermia and coupling effects. Journal of Biomechanics, 2014;47(1), 137-147.
6. Andreozzi A, Iasiello M, Netti PA. Effects of pulsating heat source on interstitial fluid transport in tumour tissues. Journal of the Royal Society Interface, 2020;17(170), 20200612.
7. Yokoyama K, Nakagawa H, Shah DC, Lambert H, Leo G, Aeby N, Ikeda A, Pitha JV, Sharma T, Lazzara R, Jackman WM. Novel contact force sensor incorporated in irrigated radiofrequency ablation catheter predicts lesion size and incidence of steam pop and thrombus. Circ Arrhythm Electrophysiol. 2008 Dec;1(5):354-62.
8. Bourier F, Popa M, Kottmaier M, Maurer S, Bahlke F, Telishevska M, Lengauer S, Koch-Büttner K, Kornmayer M, Risse E, Brkic A, Reents T, Hessling G, Deisenhofer I. RF electrode-tissue coverage significantly influences steam pop incidence and lesion size. J Cardiovasc Electrophysiol. 2021 Jun;32(6):1594-1599. doi: 10.1111/jce.15063.
9. Masnok K, Watanabe N. Catheter contact area strongly correlates with lesion area in radiofrequency cardiac ablation: an ex vivo porcine heart study. J Interv Card Electrophysiol. 2021 Sep 9. doi: 10.1007/s10840-021-01054-3.
10. Gallagher N, Fear EC, Byrd IA, Vigmond EJ. Contact geometry affects lesion formation in radio-frequency cardiac catheter ablation. PLoS One. 2013 Sep 23;8(9):e73242.
11. Tian Z, Nan Q, Nie X, Dong T, Wang R. The comparison of lesion outline and temperature field determined by different ways in atrial radiofrequency ablation. Biomed Eng Online. 2016 Dec 28;15(Suppl 2):124.
12. González-Suárez A, Berjano E. Comparative analysis of different methods of modeling the thermal effect of circulating blood flow during RF cardiac ablation. IEEE Trans Biomed Eng. 2016 Feb;63(2):250-9.
13. Pérez JJ, González-Suárez A, Berjano E. Numerical analysis of thermal impact of intramyocardial capillary blood flow during radiofrequency cardiac ablation. Int J Hyperthermia. 2018 May;34(3):243-9.
14. González-Suárez A, Pérez JJ, Berjano E. Should fluid dynamics be included in computer models of RF cardiac ablation by irrigated-tip electrodes? Biomed Eng Online. 2018 Apr 20;17(1):43.
15. Cao H, Speidel MA, Tsai JZ, Van Lysel MS, Vorperian VR, Webster JG. FEM analysis of predicting electrode-myocardium contact from RF cardiac catheter ablation system impedance. IEEE Trans Biomed Eng. 2002 Jun;49(6):520-6.
16. Petras A, Leoni M, Guerra JM, Jansson J, Gerardo-Giorda L. A computational model of open-irrigated radiofrequency catheter ablation accounting for mechanical properties of the cardiac tissue. Int J Numer Method Biomed Eng. 2019 Nov;35(11):e3232. doi: 10.1002/cnm.3232.
17. Yan S, Gu K, Wu X, Wang W. Computer simulation study on the effect of electrode-tissue contact force on thermal lesion size in cardiac radiofrequency ablation. Int J Hyperthermia. 2020;37(1):37-48. doi: 10.1080/02656736.2019.1708482.

18. Singh S, Melnik R. Computational modeling of cardiac ablation incorporating electrothermomechanical interactions. ASME J of Medical Diagnostics. 2020 Nov 2020, 3(4): 041004 (12 pages). doi: 10.1115/1.4048536.
19. Ahn JW, Kim YJ. Numerical analysis on the effects of saline injection and deformation for radiofrequency catheter ablation. Electronics 2021, 10, 1674. doi:10.3390/electronics10141674
20. Sarkozy A, Shah D, Saenen J, Sieira J, Phlips T, Boris W, Namdar M, Vrints C. Contact force in atrial fibrillation: role of atrial rhythm and ventricular contractions: co-force atrial fibrillation study. Circ Arrhythm Electrophysiol. 2015 Dec;8(6):1342-50. doi: 10.1161/CIRCEP.115.003041.
21. Gelman D, Skanes AC, Jones DL, Timofeyev M, Bar-On T, Drangova M. Eliminating the effects of motion during radiofrequency lesion delivery using a novel contact-force controller. J Cardiovasc Electrophysiol. 2019 Sep;30(9):1652-1662. doi: 10.1111/jce.14093.
22. Shah DC, Lambert H, Nakagawa H, Langenkamp A, Aeby N, Leo G. Area under the real-time contact force curve (force-time integral) predicts radiofrequency lesion size in an in vitro contractile model. J Cardiovasc Electrophysiol. 2010 Sep;21(9):1038-43. doi: 10.1111/j.1540-8167.2010.01750.x.
23. Irastorza RM, Gonzalez-Suarez A, Pérez JJ, Berjano E. Differences in applied electrical power between full thorax models and limited-domain models for RF cardiac ablation. Int J Hyperthermia. 2020;37(1):677-687. doi: 10.1080/02656736.2020.1777330.
24. Ikeda A, Nakagawa H, Lambert H, Shah DC, Fonck E, Yulzari A, Sharma T, Pitha JV, Lazzara R, Jackman WM. Relationship between catheter contact force and radiofrequency lesion size and incidence of steam pop in the beating canine heart: electrogram amplitude, impedance, and electrode temperature are poor predictors of electrode-tissue contact force and lesion size. Circ Arrhythm Electrophysiol. 2014 Dec;7(6):1174-80. doi: 10.1161/CIRCEP.113.001094.
25. González-Suárez A, Pérez JJ, Irastorza RM, D'Avila A, Berjano E. Computer modeling of radiofrequency cardiac ablation: 30 years of bioengineering research. Comput Methods Programs Biomed. 2022 Feb;214:106546. doi: 10.1016/j.cmpb.2021.106546.
26. Abraham JP, Sparrow EM. A thermal-ablation bioheat model including liquid-to-vapor phase change, pressure- and necrosis-dependent perfusion, and moisture-dependent properties. Int J Heat Mass Tran. 2007; 50(13-14):2537-2544.
27. www.matweb.com (accessed 11 June, 2021).
28. Pérez JJ, Ewertowska E, Berjano E. Computer modeling for radiofrequency bipolar ablation inside ducts and vessels: relation between pullback speed and impedance progress. Lasers Surg Med. 2020 Nov;52(9):897-906. doi: 10.1002/lsm.23230.
29. Hasgall PA, Di Gennaro F, Baumgartner C, Neufeld E, Lloyd B, Gosselin MC, Payne D, Klingenböck A, Kuster N, "IT'IS Database for thermal and electromagnetic parameters of biological tissues," Version 4.0, May 15, 2018, DOI: 10.13099/VIP21000-04-0. itis.swiss/database
30. Trujillo M, Berjano E. Review of the mathematical functions used to model the temperature dependence of electrical and thermal conductivities of biological tissue in radiofrequency ablation. Int J Hyperthermia. 2013 Sep;29(6):590-7.
31. Carson JK. Review of effective thermal conductivity models for foods. Int J Refrigeration. 2006 29(6):958-67.
32. https://www.engineeringtoolbox.com/water-properties-d_1573.html (accessed June 8, 2021).
33. Lopresto V, Argentieri A, Pinto R, Cavagnaro M. Temperature dependence of thermal properties of ex vivo liver tissue up to ablative temperatures. Phys Med Biol. 2019 May 16;64(10):105016.
34. Bhavaraju NC, Cao H, Yuan DY, Valvano JW, Webster JG. Measurement of directional thermal properties of biomaterials. IEEE Trans Biomed Eng. 2001 Feb;48(2):261-7. doi: 10.1109/10.909647.

35. Mitchell HH, Hamilton TS, Steggerda FR, Bean HW. The chemical composition of the adult human body and its bearing on the biochemistry of growth. J. Biol. Chem. 1945, 158:625-637.
36. Balduino R, McDermott B, Porter E, Adnan Elahi M, Shahzad A, O'Halloran M, Cavagnaro M. Feasibility of water content-based dielectric characterisation of biological tissues using mixture models. IEEE Trans Dielectrics Electrical Insulation. 2019. 26(1): 187-193.
37. Nakagawa H, Ikeda A, Sharma T, Govari A, Ashton J, Maffre J, Lifshitz A, Fuimaono K, Yokoyama K, Wittkampf FHM, Jackman WM. Comparison of In Vivo Tissue Temperature Profile and Lesion Geometry for Radiofrequency Ablation With High Power-Short Duration and Moderate Power-Moderate Duration: Effects of Thermal Latency and Contact Force on Lesion Formation. Circ Arrhythm Electrophysiol. 2021 Jul;14(7):e009899. doi: 10.1161/CIRCEP.121.009899.
38. Wildlund OB, Keyes DE. Domain decomposition methods in science and engineering XVI (Wildlund OB, Keyes DE, Eds.). Springer. 2007. doi: 10.1007/978-3-540-34469-8.
39. Pérez JJ, González-Suárez A, Nadal E, Berjano E. Thermal impact of replacing constant voltage by low-frequency sine wave voltage in RF ablation computer modeling. Comput Methods Programs Biomed. 2020 Oct;195:105673. doi: 10.1016/j.cmpb.2020.105673.
40. Leshem E, Tschabrunn CM, Contreras-Valdes FM, Zilberman I, Anter E. Evaluation of ablation catheter technology: Comparison between thigh preparation model and an in vivo beating heart. Heart Rhythm. 2017 Aug;14(8):1234-1240. doi: 10.1016/j.hrthm.2017.04.035.
41. Guerra JM, Jorge E, Raga S, Gálvez-Montón C, Alonso-Martín C, Rodríguez-Font E, Cinca J, Viñolas X. Effects of open-irrigated Radiofrequency ablation catheter design on lesion formation and complications: in vitro comparison of 6 different devices. J Cardiovasc Electrophysiol. 2013 Oct;24(10):1157-62. doi: 10.1111/jce.12175.
42. Perna F, Heist EK, Danik SB, Barrett CD, Ruskin JN, Mansour M. Assessment of catheter tip contact force resulting in cardiac perforation in swine atria using force sensing technology. Circ Arrhythm Electrophysiol. 2011 Apr;4(2):218-24. doi: 10.1161/CIRCEP.110.959429.
43. Kalman JM, Fitzpatrick AP, Olgin JE, Chin MC, Lee RJ, Scheinman MM, Lesh MD. Biophysical characteristics of radiofrequency lesion formation in vivo: dynamics of catheter tip-tissue contact evaluated by intracardiac echocardiography. Am Heart J. 1997 Jan;133(1):8-18. doi: 10.1016/s0002-8703(97)70242-4.
44. Chik WW, Barry MA, Pouliopoulos J, Byth K, Midekin C, Bhaskaran A, Sivagangabalan G, Thomas SP, Ross DL, McEwan A, Kovoor P, Thiagalingam A. Electrogram-gated radiofrequency ablations with duty cycle power delivery negate effects of ablation catheter motion. Circ Arrhythm Electrophysiol. 2014 Oct;7(5):920-8. doi: 10.1161/CIRCEP.113.001112.
45. Ramadan S, Paul N, Naguib HE. Standardized static and dynamic evaluation of myocardial tissue properties. Biomed Mater. 2017 Mar 20;12(2):025013. doi: 10.1088/1748-605X/aa57a5.

Table 1. Thermal and electrical characteristics of the elements employed in the model.

Element/Material	σ **(S/m)**	k **(W/m·K)**	ρ **(kg/m^3)**	c **(J/kg·K)**
Electrode/Pt-Ir [28]	4.6×10^{6}	71	21500	132
Catheter/Polyurethane [28]	10^{-5}	23	1440	1050
Cardiac Chamber/Blood [29]	0.748	–	–	–
Myocardium (hydrated [29])	0.281	0.56	1081	3686
Myocardium (dehydrated)*	0.007	0.287	1428	2474

σ, electrical conductivity (at 500 kHz); k, thermal conductivity; ρ, density; and c, specific heat (all assessed at 37 ºC in case of tissue and blood). * Estimated (see text and Appendix for details). Thermal problem was not solved in the blood subdomain.

Table 2. Depth (D), maximum width (MW) and surface width (SW) of lesions computed with the electrode inserted in the tissue and withdrawn for static and dynamic cases (20 W, 30 s).

CASES	Contact force (g)	Inserted (t = 63 s)			Withdrawn (t = 62 s)		
		D (mm)	MW (mm)	SW (mm)	D (mm)	MW (mm)	SW (mm)
Static	10	5.31	8.64	6.48	5.21	8.60	6.54
	20	6.00	9.46	6.98	5.79	9.38	7.04
	30	6.64	10.22	7.44	6.36	10.10	7.52
Dynamic	20 ± 10	6.04	9.48	6.98	5.83	9.38	7.04

Table 3. Comparison of computer (dynamic case) and experimental (beating heart model) results in terms of lesion size (D: depth, MW: Maximum width, SW: surface width).

	Conditions (Contact Force, Power – duration)	**D (mm)**	**MW (mm)**	**SW (mm)**
Computer results*	20 ± 10 g, 25 W–30 s	6.01±0.07	9.46±0.18	6.98±0.16
Ikeda *et al* [24]	22 g, 30 W–60 s	6.7±0.8	9.6±1.1	7.2±0.6
Leshem *et al* [40]	10 g, 30 W–30 s	5.95±1.3	8.99±2.1	–
Nakawaga *et al* [37]	18.1±7.6 g, 30 W–30 s	5.6±1.4	8.7±1.7	7.3±1.1

* Case of inserted electrode

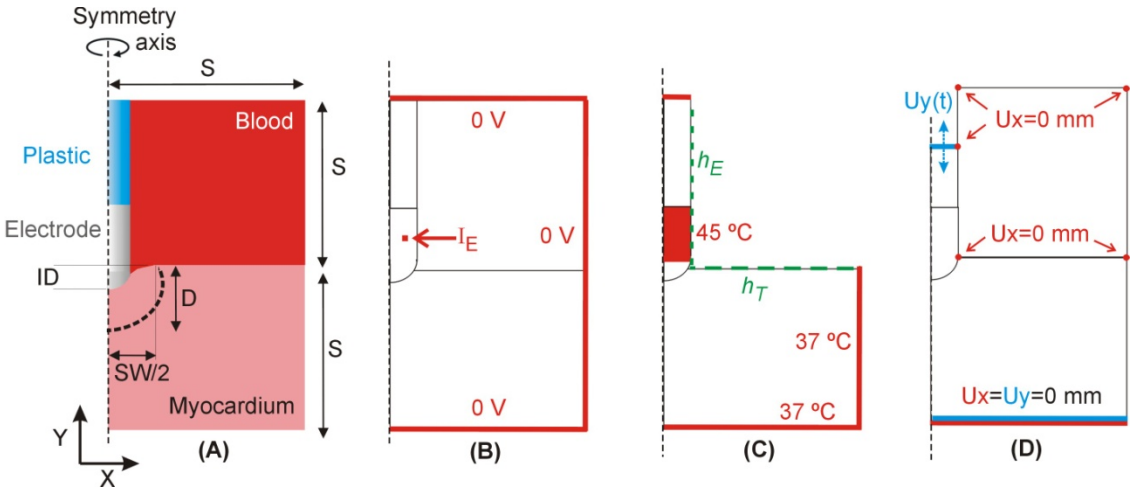

Figure 1 **A:** Geometry of the two-dimensional computational model built (not to scale) including an ablation electrode (7Fr, 4 mm) inserted into a fragment of myocardium and completely surrounded by blood. Dimension of myocardium and blood (S) is obtained from a convergence test. **B:** Electrical boundary conditions. The axial symmetry implies that the x-component of the current density is zero on the axis. **C:** Thermal boundary conditions (blood excluded). h_E and h_T are the thermal convection coefficients at the electrode–blood and tissue–blood interfaces, respectively. The axial symmetry implies that the x-component of the heat flow is zero on the axis. **D:** Mechanical boundary conditions of displacement (x-component in red and y-component in blue).

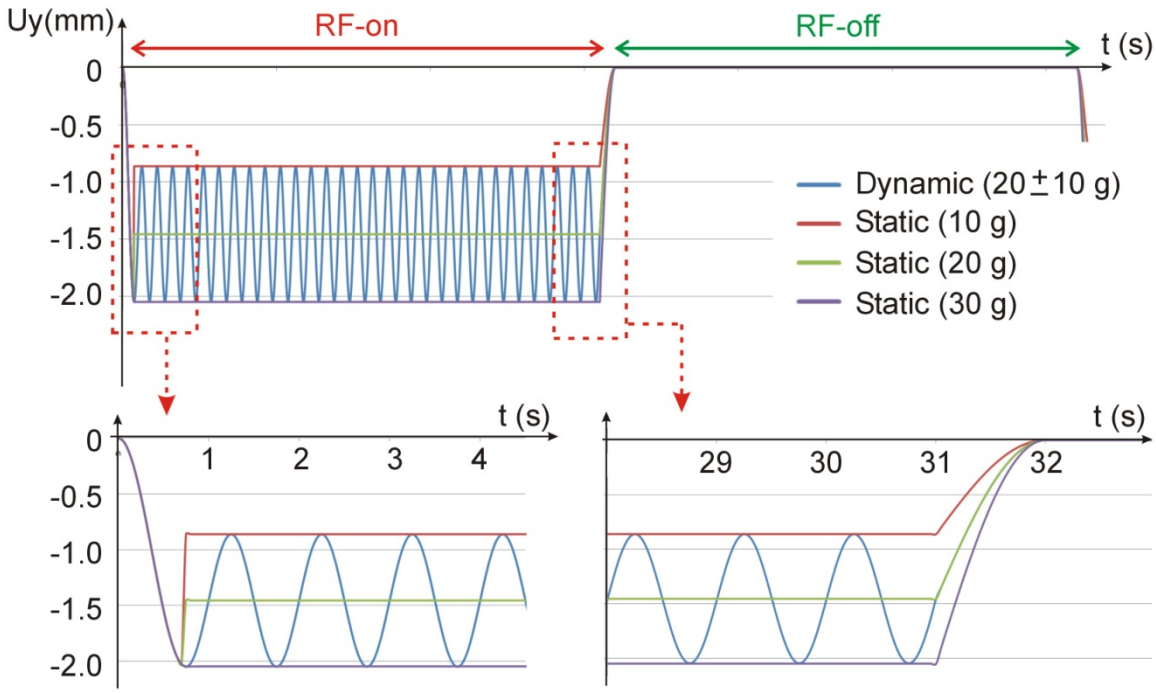

Figure 2 Evolution of the y-component of the displacement (Uy) applied as a mechanical load on the catheter during the ablation time (RF-on) and post-ablation time (RF-off) for static and dynamic case and different values of contact forces.

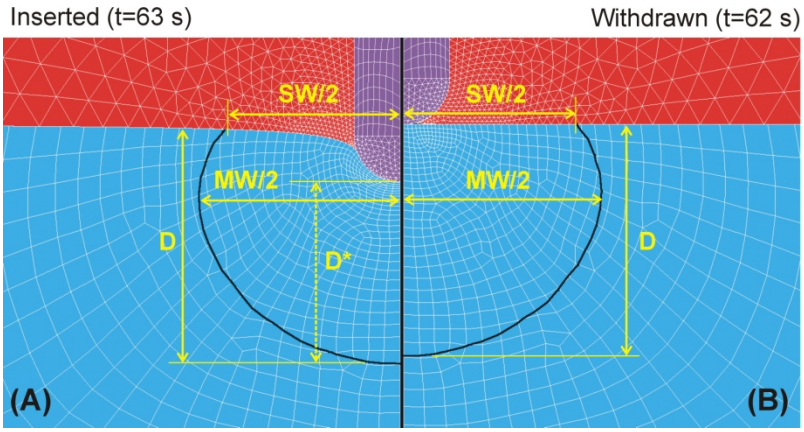

Figure 3 Thermal lesion contour computed with Arrhenius damage model ($\Omega = 1$) for electrode inserted (A) and withdrawn (B), both after the post-RF period. SW: surface width, MW: Maximum width, D: depth from tissue surface, and D*: depth from electrode tip (only in Case A).

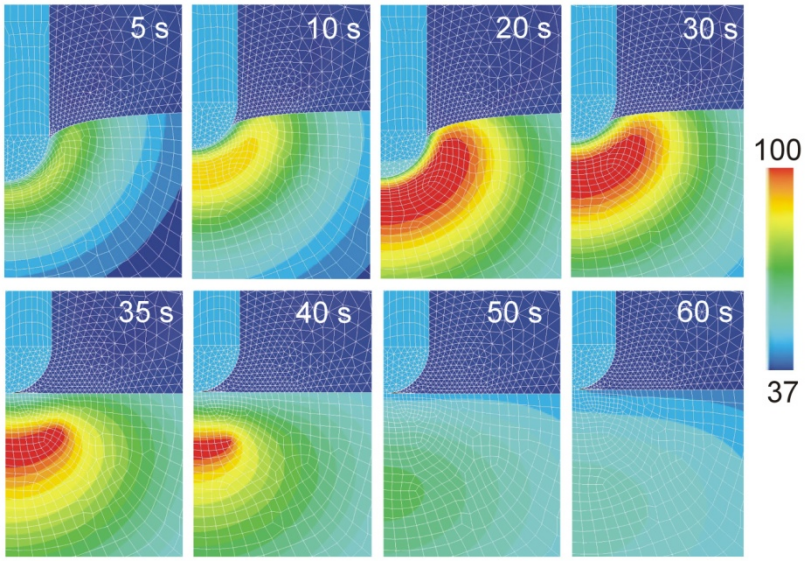

Figure 4 Temperature distributions in the tissue at different ablation times (5, 10, 20 and 30 s) and post-ablation period (35, 40, 50 and 60 s). The plots are those of different electrode positions within its vertical displacement in the dynamic case with a CF of 20±10 g. Scale in ºC.